Analysis of Disk Brake Creep Groan Vibrations at Automobile Chassis Front Corner Level Using High-Speed Recordings and Digital Image Processing

Manuel Pürscher and Peter Fischer

Abstract Automobile brake creep groan denotes self-excited vibro-acoustic effects during a cross-fade of moderate brake pressures with slow vehicle velocities near standstill. Friction-induced creep groan phenomena are perceived inside and outside a passenger car. The mainly emphasized structure-borne low-frequency range extends up to about 400 Hz. Although creep groan is technically harmless, it attracts increasing attention in customer-focused assessments of comfort, reliability and safety. In view of this acute product quality problem, effective countermeasures must be developed based on a holistic understanding. The present work supports this challenging task by means of unique experimental investigations. These relate to an exemplary MacPherson-type front axle setup including floating caliper disk brake system. Realistic creep groan vibrations are provoked and sustained via a drum-driven chassis corner test rig. Two representative manifestations at similar brake pressures and drum velocities are analyzed in particular. Apart from conventional caliper acceleration and disk rotation measurements, a low-cost high-speed camera is pointed to the friction system. It vividly reveals mechanisms which are invisible to the human eye. A processing strategy for the picture series is created. It enables object tracking and stick–slip recognition. Results obtained thereby correlate with the analyzed sensor data. The basic creep groan frequency is around 22 or 87 Hz here. Both periodic nonlinear vibrations rely on macroscopic stick–slip transitions of the friction pair which interact with characteristic inherent resonances of different chassis corner components. Eventually, this case study proofs that the adopted non-contact method is helpful to better comprehend creep groan phenomena.

Keywords Creep groan · High-speed video · Digital image correlation · Test rig

M. Pürscher (✉) · P. Fischer
Institute of Automotive Engineering, Graz University of Technology, Inffeldgasse 11/2, 8010 Graz, Austria
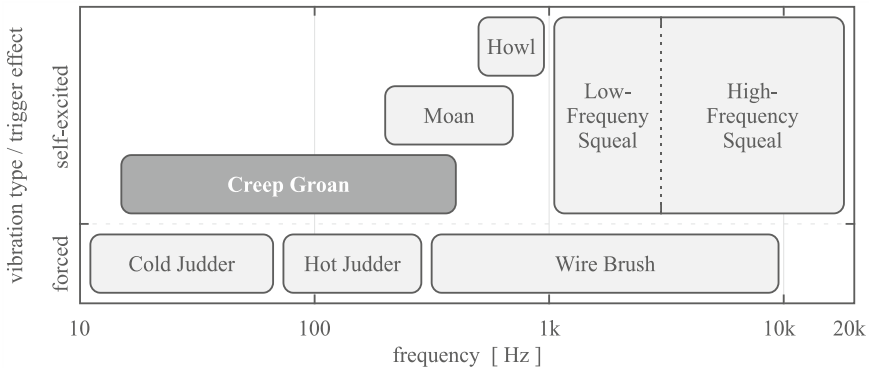e-mail: m.puerscher@tugraz.at

Fig. 1 Typical disk brake NVH classification: excitation mechanism over frequency range

1 Introduction

1.1 *Vibro-Acoustic Emissions of Automobile Brakes*

Barden [1] has outlined a long-term relevance of the vibro-acoustic properties for the subconscious product experience. This strongly applies to high-tech products such as automobiles. Consequently, automotive companies must meet stringent customer-focused requirements on noise, vibration and harshness (NVH) across all vehicle segments.

NVH originating in the friction brake system leads to an impaired overall rating of comfort and quality in particular. Moreover, drivers and occupants as well as individuals outside an affected passenger car loose trust in its reliability and safety. Accordingly, brake NVH problems often stand out in customer-focused satisfaction surveys (e.g. [2–4]). Immediate costly consequences of these technically, mostly harmless, vibro-acoustic issues are warranty claims.

From a bandwidth of known disk brake NVH phenomena, see coarse classification in Fig. 1, the so-called brake creep groan is of interest within this work. This tactile and audible self-excited low-frequency problem has lately gained higher topicality. In the following, reasons as well as phenomenological aspects are described based on acknowledged literature [5–14] and own studies such as [15–17].

1.2 *Creep Groan Phenomena*

Creep groan shows up during a cross-fade of moderate brake pressures up to about 30 bar with very slow vehicle (wheel) velocities up to about 0.30 km/h.

Automobiles with torque converter have always been prone to creep groan phenomena. A blending of both mentioned operational parameters is typical during

a normal move-off from standstill. This is why brake creep groan has been problematic in markets with a long-term dominance of automatic transmissions at first, for example, North America or Japan. If the brake system is active during a slow roll-off at inclines or during a steering at standstill, creep groan may appear for any powertrain architecture. Beyond that, the so-called dynamic groan is a partly similar vibroacoustic effect of less relevance which occasionally shows up during deceleration shortly prior to a halt. Nowadays, creep groan is problematic in markets worldwide. On one hand, this is caused by grown sales shares of torque converter passenger cars, increased quality expectations and diminished NVH masking of optimized aggregates. On the other hand, progressive drivetrain electrification and advanced driver assistance systems encourage the incidence of creep groan phenomena. The characteristic operational parameter blending is not only obligatory for an ordinary start-up from standstill, but also for semi-autonomous modes such as stop-and-go-chauffeur or remote-parking.

Independent of the vehicle, the physical nature of friction-induced creep groan requires similar competing levels of drive torque and brake torque as well as different coefficients of static and dynamic friction. These conditions favor two alternating tribological states between pad linings and disk surface. The stick phase causes a system pretension with large displacements. The slip phase enables a contrary relaxation. Accordingly, creep groan relies on a self-excited stick–slip mechanism. Each abrupt macroscopic transition from stick to slip excites natural oscillations of the surrounding chassis corner components. Certain inherent low-frequency resonances contribute to the impulsive nonlinear oscillations in particular. Hence, periodic vibrations during persistent creep groan contain frequency contents, which clearly exceed the major stick–slip interval or basic vibration frequency, respectively. The structure-borne frequency range including super-harmonics is often mentioned from approximately 15–400 Hz.

1.3   2-D Digital Image Correlation (DIC) in Applied Engineering

The great potential of picture series for the study of visually observable transient effects was recognized in the field of applied engineering more than 100 years ago. Beyond that, analog high-speed video techniques expanded the possibilities from the 1940s onwards. A technical application example was given by Hawkins [18] as early as the 1950s. He quantified structural surface accelerations via analog high-speed recordings. The advances made in the following decades led to better film equipment and digitized images, as well as mathematical and computational foundations of 2-D DIC which emerged in the field of applied engineering in the early 1980s. Nowadays, commercial software tools as well as open source codes are available; see DIC package overview of Belloni et al. [19]. Mind that the generic term DIC summarizes

various methods or algorithms, for example, procedures based on normalized cross correlation (NCC).

The DIC is an established non-interferometric approach in the field of experimental solid mechanics; see extensive bibliography collected from Orteu [20]. The method is also used for displacement analyses concerning vibrations or stick–slip mechanisms. These universal problems occur in diverse research areas such as civil, mechanical, geological, biomedical or sound engineering, compared to representative works [12, 21–28]. Ferrer et al. [21] analyzed vibrations of a pedestrian bridge. Hedayat and Ashur [22] evaluated deformations of wood structures under compression. Tuononen [23] examined the variable stick–slip behavior of rubber tread blocks on a glass plate to better comprehend the road contact of a vehicle tire. Pesaresi et al. [24] analyzed kinematics and stick–slip mechanisms of a passive friction damper designed for turbine applications. Daoud et al. [25] evaluated the stick–slip behavior of granular materials during an initiated shear failure. Rudolf et al. [26] examined stick–slip mechanisms concerning seismotectonic scale models by means of a sophisticated monitoring system. Nonomura et al. [27] analyzed stick–slip relative movements between human fingertips and a moistened glass plate for conclusions on the tactile sense. Van Karsen et al. [28] evaluated stick–slip behavior and wave propagation regarding a bowed violin string.

Although 2-D DIC is well-accepted in applied engineering, it is still unconventional in research and development on friction brake systems. Only two publications concerning pad lining characterization were found. Kawabe [29] studied the inhomogeneous compressibility for different ingredients and Dufrenoy [30] analyzed the nonlinear mechanical properties for different compounds. Of course, their DIC methods do not require high-speed recordings. Surprisingly, Gieck [31] examined vehicle brake noise phenomena via analog high-speed videos as early as the 1950s when DIC was still futuristic. In more recent years, Degenstein [32] deduced the outer pad's quasi-static displacements during vibration-free brake actuations by means of simple manual measurements in digital low-speed picture series, and furthermore, Augsburg et al. [12] carried out systematic DIC analyses at brake system level based on digital high-speed videos. This group processed picture series of disk, caliper, pad linings and friction area sections during stick–slip associated vibrations.

1.4   Normalized Cross Correlation (NCC)

Lewis [33] as well as Briechle and Hanebeck [34] mentioned signal cross correlation as standard metric for feature matching based on the convolution theorem. The efficient computation in the spectral domain rests on the fast Fourier transform (FFT). In the spatial domain, template matching or feature tracking is possible via the NCC principle. Certainly, other different methods are available, for example, active contour matching, fast convolution, gradient descent search, multi resolution search, phase correlation, sequential similarity detection, and so on. However, a given NCC

function denoted as `normxcorr2(...)` is available in the commercial software 'MATLAB R2014b' which is deployed within this work.

The NCC principle for DIC feature matching rests on the squared Euclidian distance metric, see definition in Eq. (1) and [33]. Accordingly, p is an unregistered 2-D picture of interest and the sum is over x, y under the window with a predefined 2-D template t at the variable position (u, v).

$$d_{p,t}^2(u, v) = \sum_{x,y} [p(x, y) - t(x - u, y - v)]^2 \tag{1}$$

In expansion, the template energy term $\sum_{x,y} t^2(x - u, y - v)$ is constant. If the picture energy term $\sum_{x,y} p^2(x, y)$ is nearly constant, $\sum_{x,y} [2 \cdot p(x, y) \cdot t(x - u, y - v)]$ quantifies the similarity between picture and template. To overcome disadvantages of this affinity metric, for example, caused by changes in brightness, contrast, colors or quality of unregistered pictures regarding a template, a normalization to unit length is appropriate. It yields a more meaningful coefficient with values from -1 to $+1$, see definition in Eq. (2) and [33, 34]. It involves $p_{u,v}$ as the mean value of $p(x, y)$ within the area under the movable window positioned at (u, v) and $\bar{t}$ as the constant mean value of the template.

$$\text{NCC}(u, v) = \frac{\sum_{x,y} \{[p(x, y) - \overline{p}_{u,v}] \cdot [t(x - u, y - v) - \bar{t}]\}}{\sqrt{\sum_{x,y} [p(x, y) - \overline{p}_{u,v}]^2 \cdot \sum_{x,y} [t(x - u, y - v) - \bar{t}]^2}} \tag{2}$$

If the template is systematically moved in both directions over the picture, Eq. (2) leads to an NCC matrix, which includes a maximal positive-valued entry on the coordinate with the best similarity to the template, compared to explanations in [33, 34].

1.5 Context and Content of This Paper

Compared to the well-studied universal stick–slip effect, brake creep groan offers greater research potential. Around 200 publications on creep groan can be found. First industrial papers date from the 1980s, for example the work of Schwartz et al. [5]. They have focused on elementary on-road tests. The following decade spawned scientific reports including more detailed full vehicle measurements and/or simple dynamometer test bench investigations (e.g. [6–8]). In addition, simulations based on relatively small stick–slip oscillator systems are documented from this period (see [6, 7]). More recent efforts of industry and university often treat on-road measurements, test rig experiments at different module levels and/or friction pair benchmarks (e.g. [9–14]). Moreover, simulative investigations at various problem

levels have gained relevance (see [9, 10, 13, 14]). This extends up to 3-D finite element (FE) models, compared to suggestion in [13].

Nowadays, automobile brake engineers are looking for expedient combinations of subsystem test procedures with equivalent virtual methods to eliminate creep groan during the product development phase. For this purpose, the authors of this work have already presented appropriate investigation methods. First is an operational parameter matrix procedure [15]. It is performed on a drum-driven chassis corner test rig. Second is a transient simulation approach [16, 17]. It computes a nonlinear 3-D FE model of front axle setup, including disk brake system, to evaluate creep groan vibrations akin to the experiments.

The current work deals with unique experimental brake creep groan investigations at automobile chassis front corner level. The realization of a non-contact DIC approach is discussed. Recordings of an affordable digital high-speed camera, which is pointed to the friction system, are analyzed. The elaborated method aims at a better understanding of creep groan phenomena or other low-frequency brake NVH issues alike. Accordingly, countermeasures may be developed based on more detailed knowledge.

2 Experiments

2.1 Chassis Corner Test Rig Application

The drum-driven chassis corner test rig illustrated in Fig. 2 is deployed. It is located at the 'Institute of Automotive Engineering' in Graz, Austria. The machine stands in an air-conditioned and sound-isolated chamber. In operation, the hydraulically applied vertical loading maintains the vehicle corner's defined in situ height. Thus, a realistic pretension of all axle and suspension components is achieved. The drive torque is not directly adjusted. However, brake pressure and drum (wheel) velocity
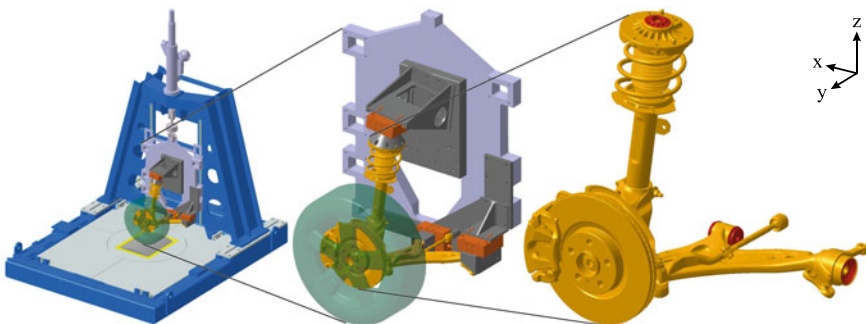

Fig. 2 Drum-driven chassis corner test rig with MacPherson-type front axle setup including floating caliper disk brake system

are under control. Both operational parameters are adjusted with an 100 Hz rate. More information on the versatile test facility is included in former publications such as [15–17].

The test specimen from a compact van is a MacPherson-type front axle suspension assembly (see Fig. 2). It includes a front-mounted single-piston floating caliper brake system. The 330 mm cast iron monobloc disk, as well as the pad linings, is designated for the European market. The chassis corner setup from the left side with roughly 55 kg overall mass is attached to the test rig's vertical interface plate according to known vehicle body dimensions. Two steel adapters at the lower control arm bushings as well as one console above the suspension strut support contain cuboid form load cells, respectively. The track rod's spherical joint is also connected to the interface plate. The anti-roll bar is not relevant here. Since a drive shaft is not included in this application, a 17" wheel is turned exclusively from the drum.

2.2 High-Speed Recordings

Positioning and specification of the deployed low-cost film equipment can be seen in Fig. 3. The 6 Megapixel (Mpx) camera was launched in 2008 for around $1000. In the fastest high-speed mode, it achieves 1200 frames per second (fps) in a maximal image resolution of 336×96 px.

Camera and spotlight are directed to the inlet side of the friction system. A suitable daylight headlamp is important for consistently well-illuminated picture series. The outer disk edge, which is not part of the friction surface, is speckled by means of a permanent marker akin to the dots at the disk in [12]. Since caliper anchor and both pad linings most likely move as coupled rigid body during creep groan, caliper anchor images are analyzed instead of the invisible leading edge of the outer pad lining.
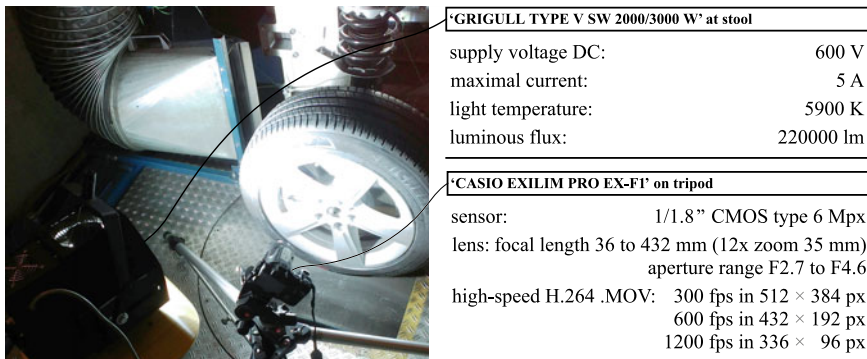

'GRIGULL TYPE V SW 2000/3000 W' at stool	
supply voltage DC:	600 V
maximal current:	5 A
light temperature:	5900 K
luminous flux:	220000 lm

'CASIO EXILIM PRO EX-F1' on tripod	
sensor:	1/1.8" CMOS type 6 Mpx
lens: focal length 36 to 432 mm (12x zoom 35 mm)	
	aperture range F2.7 to F4.6
high-speed H.264 .MOV:	300 fps in 512×384 px
	600 fps in 432×192 px
	1200 fps in 336×96 px

Fig. 3 Positioning and specification of the equipment for high-speed video recordings

Fig. 4 Triaxial accelerometer mounted on caliper anchor and miniature rotation encoder with rubber ring pulley running on rim well

2.3 Conventional Measurements

The two relevant traditional sensors at the test specimen are depicted in Fig. 4. On one hand, the x- and z-direction of the triaxial accelerometer 'PCB 356A02' on the caliper anchor are processed. The sensor delivers reasonable analog signals from roughly 1–3000 Hz to the 'DEWETRON DEWE-501' data acquisition system which has a low-pass filter activated. It acquires the data with a temporal resolution of 10,000 samples per second (sps). On the other hand, signals of the rotation encoder 'SCANCON SCA24-5000' are recorded. The rotation encoder is with a rubber ring pulley in slightly preloaded contact to the rim well. Each revolution of the 17" wheel is resolved with roughly 65,200 increments. The fabricated bracket of the sensor is supported from the wheel bearing housing.

2.4 Creep Groan Test Matrix Approach

The drum-driven chassis corner test rig is used to reproducibly stimulate creep groan vibrations in dependence of brake pressures and drum velocities. For this purpose, a customizable test matrix procedure has been introduced in [15]. Accordingly, measured caliper accelerations are deterministically analyzed in terms of spectral content and vibration energy. A developed algorithm determines for each matrix item whether its acceleration signal refers to brake creep groan. If so, the vibration frequency which most likely indicates the fundamental stick–slip interval is picked out. Finally, a so-called creep groan map (CGM) is the evaluation output.

The test specimen's simplified CGM with 190 operational parameter settings is shown in Fig. 5. This simplified CGM from 4 to 40 bar and 0.04 to 0.40 km/h is valid for a specific configuration of the corporeal components. Since chamber air, as well as cooling air, is conditioned, the temperature of the friction couple remains stable at 20–35 °C. Note that other tribological influences, for example, thermal
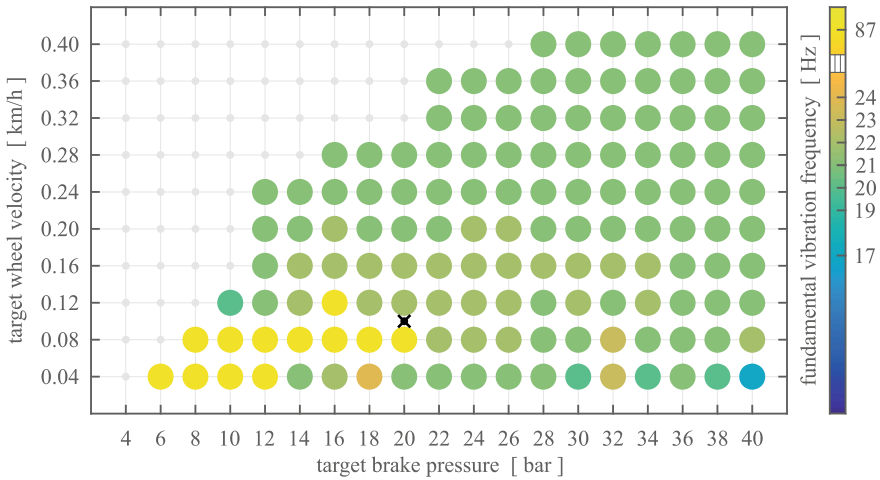
Fig. 5 Relevant simplified CGM of 190 operational parameter combinations with basic creep groan vibration frequencies hinted via large colored circles

loads, progressive wear or temporary water exposure, are not taken into account in the initial implementation of the systematic procedure.

Large shaded circles in Fig. 5 represent persistent creep groan. Colors indicate the basic stick–slip frequency, which is around 22 and 87 Hz here. The nonlinear leap between these two characteristic frequency regions marks operational parameter settings with a bifurcation tendency, compare explanations with [14]. Bifurcation in the present context means that more than one type of brake creep groan is alternatively manifested, for example, 20 bar at 0.10 km/h. Both periodic nonlinear vibration phenomena at this representative operational parameter combination are analyzed within this work.

3 Analyses

3.1 Digital Image Processing Sequence

A customizable processing sequence has been created to analyze the high-speed videos of the interacting brake system friction couple. In the following, mainly relevant elements are explained.

Defining temporal segment of interest. An 1 s high-speed video segment is manually preselected to be in sync with a prechosen 1 s measurement data segment of the same creep groan experiment.
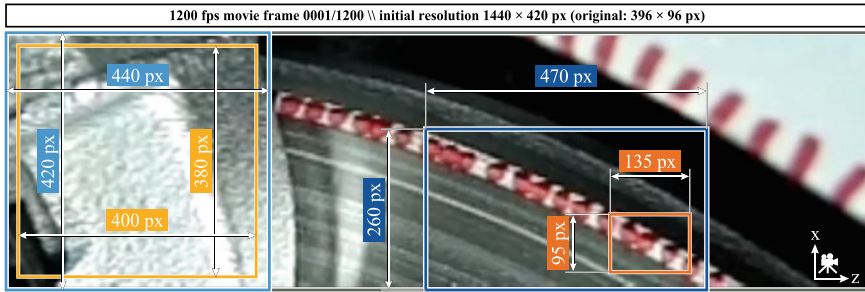
Fig. 6 First of 1200 fps movie frames with initial-field, trimmed-fields (outside) and template-fields (inside) at caliper anchor and outer disk edge, respectively

Enlarging video resolution. The 336×96 px original video is truncated and formatted into an undistorted 1440×1080 px high-definition video by means of the freely available software 'MICROSOFT Windows Movie Maker Version 2012'. Note that the new picture series of the 1 s segment has black borders at the top and bottom.

Determining visual areas of interest. Sizes and positions of so-named initial-field, trimmed-fields and template-fields have to be preselected for two evaluation threads (see Fig. 6). The initial-field ought to cut the black borders. Trimmed-fields should define narrowed problem areas to lower the computational effort. The small template-fields determine distinctive local reference problem areas which must not leave the fixed trimmed-fields during an entire 1 s segment of tracking.

Performing digital image processing sequence. The commercial software 'MATLAB R2014b' includes proper native functions for digital image processing and data analysis. These must be adjusted and arranged to a suitable picture series editing sequence which is hinted in Fig. 7 for the temporal boundary frames of an exemplary 1200 fps movie. Firstly, the 4:3 high-definition video is loaded to the workspace through the function `VideoReader(...)`. Subsequently, a template reference is prepared and a loop for its tracking is iterated.

Template Reference Preparation. The steps to successfully obtain a template reference for an ensuing tracking loop algorithm are concatenated as follows:

- Extracting the three red-green-blue (RGB) color model matrices of a relevant 1440×1080 px high-definition video frame with `readFrame(...)`.
- Cropping the three matrices to the initial-field 1440×420 px by means of `imcrop(...)`, see Ⓐ and ⓐ in Fig. 7.
- Cutting two positioned trimmed-fields of size 440×420 px and 470×260 px out of each matrix through `imcrop(...)`, compare Ⓑ and ⓑ.
- Adjusting the RGB color component values for an improved contrast with `imadjust(...)`, see Ⓒ and ⓒ in Fig. 7.
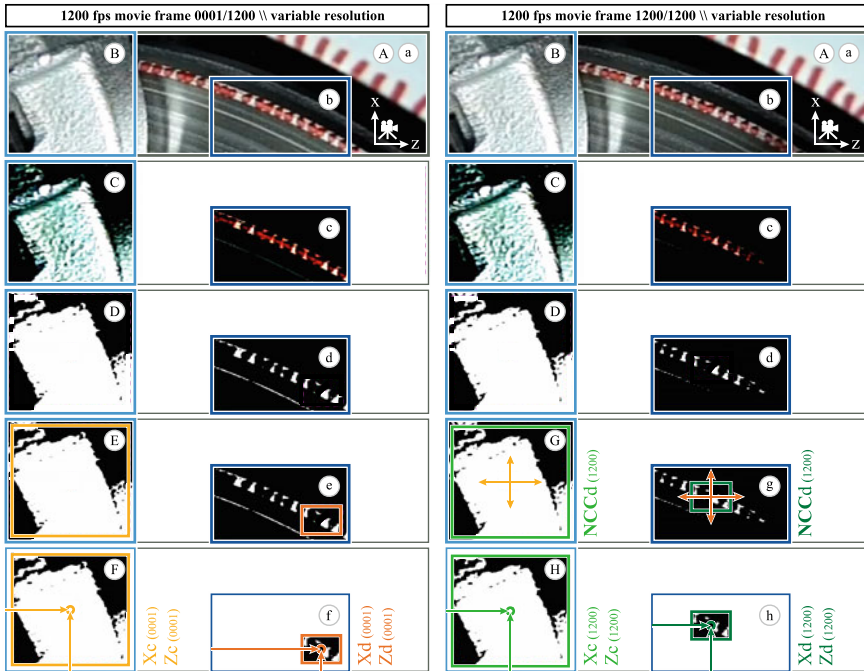
Fig. 7 Picture series editing sequence of first (left) and last (right) of 1200 fps movie frames with predefined visual areas of interest at caliper anchor and outer disk edge, respectively

- Converting the adjusted trimmed-field RGB matrices into binary matrices and removing adjacent non-zero (white) objects less than 1000 px in the three binary caliper anchor images and smaller than 3 px in each disk edge image by means of bwareaopen(...).
- Combining exclusively entries with non-zero values in all three coarsened binary matrices leads to two cumulative black-and-white images, compare (D) and (d).
- Cropping template-fields of size 400 × 380 px and 135 × 95 px out of the two cumulative binary matrices through imcrop(...), see (E) and (e) in Fig. 7.
- Scaling both template references to 800 × 760 px and 270 × 190 px via bilinear interpolation with imresize(...).
- Zeroing the first tracking vector entries Xc (0001) and Zc (0001) of caliper anchor as well as Xd (0001) and Zd (0001) of disk edge, compare to (F) and (f).

Template Tracking Loop. The sequence from (A) or (a) to (D) or (d) is repeated for each of 1199 remaining unregistered frames. Certainly, the iteration involves other steps, e.g. DIC calculation. These are summarized as follows:

- Enlarging both current cumulative binary matrices to 880 × 840 px and 940 × 520 px via bilinear interpolation by means of imresize(...).

- Computing NCC from interpolated trimmed up-to-date binary matrices to the corresponding scaled template references yields matrices **NCC**c (frame) and **NCC**d (frame) of size 1679×1599 px and 1209×709 px including values from -1 to $+1$ through `normxcorr2(...)`, see Ⓖ and ⓖ in Fig. 7.
- Identifying maximal positive-valued entries in **NCC**c (frame) and **NCC**d (frame) with `max(max(...))`.
- Locating adequate positions in the interpolated trimmed up-to-date images for leveling the current tracking vector entries Xc (frame) and Zc (frame) as well as Xd (frame) and Zd (frame) to the first entries, compare Ⓗ and ⓗ.
- Halving the current tracking vector entries to recoup scales used prior to the bilinear interpolation.

The computational effort of the digital image processing sequence for caliper anchor as well as disk edge is roughly 1300 s in total. The deployed laptop with a processor 'INTEL quad core i7' clocked at 2.5 GHz and a working memory of 8 GB RAM runs the operating system 'MICROSOFT Windows 7 SP1 64 Bit'.

Analyzing Deduced Data. The analysis of the obtained tracking vector data for exactly 1 s of filmed brake creep groan is two-fold. Firstly, caliper anchor and disk edge are considered separately. Secondly, data of both tracking vectors are merged to a relative movement for conclusions on the friction pair's stick–slip behavior.

1200 fps DIC Separate Template Tracking. The maximal NCC gives information about the specific reliability of both DIC implementations. The ascending calculation of Xc (frame)−Xc (0001) or Xd (frame)−Xd (0001) in x-direction and Zc (frame)−Zc (0001) or Zd (frame)−Zd (0001) in z-direction hints at local movements concerning prechosen temporal starting points at arbitrary spatial starting locations which are shifted to zero.

1200 fps DIC Relative Template Tracking. The separate calculations regarding caliper and disk are subtracted from one another in x- and z-direction, respectively. The geometrical sum of both spatial differences forms a combined disk to caliper relative xz-movement vector with entries denoted as XZdc (frame). Ascending absolute values according to |XZdc (frame)|−|XZdc (0001)| as well as successive values based on |XZdc (frame)|−|XZdc (frame−1)| are analyzed. Moreover, a centered five-point moving average filter smoothens the successive xz-movement values and a Hanning window weighting FFT delivers a Root Mean Square (RMS) frequency content from 1 to 240 Hz in 1 Hz intervals.

3.2 Data Processing for Caliper Acceleration and Disk Rotation

Analyzing Measured Data. The analysis of exactly 1 s of measured creep groan in sync with the high-speed video intends qualitatively coequal results. On one hand, the acceleration on the caliper anchor is considered for statements on nonlinear vibration

patterns. On the other hand, the rotation of the disk with rim is analyzed for findings on actual stick–slip intervals.

10000 sps Accelerations. The measurements with a total duration of approximately 24 s begin and end at the test specimen's rest position, compared to experimental modality described in [15]. Hence, it is justified to subtract static offsets in the 10,000 sps acceleration raw data. The obtained x- and z-accelerations allow basic interpretations here. Caliper anchor displacements are meaningful alike. Therefore, the offset-corrected accelerations are damped outside the frequency range from 5 to 2500 Hz. Two Hamming window weighting feedforward filters are used. These are a 200th-order low-pass finite impulse response (FIR) filter and a 2000th-order high-pass FIR filter. Additional applications to the reverse signal directions circumvent phase shift errors. Subsequently, numerical time integral formulas are used. The velocity vector $v(k)$ for the data points k is estimated from the filtered acceleration vector $a(k)$ via a trapezoidal rule according to $v(k + 1) = v(k) + [a(k) + a(k + 1)]/2 \cdot (1/10,000)$. The displacement vector $s(k)$ rests on $s(k + 1) = s(k) + [v(k) + v(k + 1)]/2 \cdot (1/10,000)$. The mentioned rest position provides known initial conditions. Offset correction is also performed in between the two time integral approximations. Since only the 10,000 values during a preselected 1 s sequence are of interest, the spatial starting location of the first relevant entry in $s(k)$ denoted as s (sample) is shifted to zero. Thus, local x- and z-displacement are available.

Resampled 1200 sps Rotation. The 10,000 sps rotation encoder raw data is resampled to 1200 sps by means of the function `interp1(...)` applied for linear interpolation. A given transmission ratio of 65.2:5 is used to deduce a rotation angle vector $\Phi(k)$ of the disk with rim. Its entries Φ (sample) are considered in minutes of arc. Since only the resampled 1200 values during a preselected 1 s sequence are of interest, the first entry is set to zero. Ascending absolute values |Φ (sample)|–|Φ (0001)| as well as successive values |Φ (sample)|–|Φ (sample−1)| are relevant. Moreover, a centered five-point moving average filter smoothens the successive rotation angle values and a Hanning window weighting FFT delivers a RMS frequency content from 1 to 240 Hz.

4 Results

4.1 Basic Vibration Frequency 22 Hz—Non-contact Approach

Results of the non-contact approach in Figs. 8, 9, 10 and 11 relate to a persistent 22 Hz creep groan phenomenon of the test specimen. It appeared in corner test rig experiments at 20 bar brake pressure with 0.10 km/h drum velocity.

1200 fps DIC Separate Template Tracking. As one can see in Fig. 8, a consistently high maximal NCC concerning the caliper anchor picture series indicates a reliable
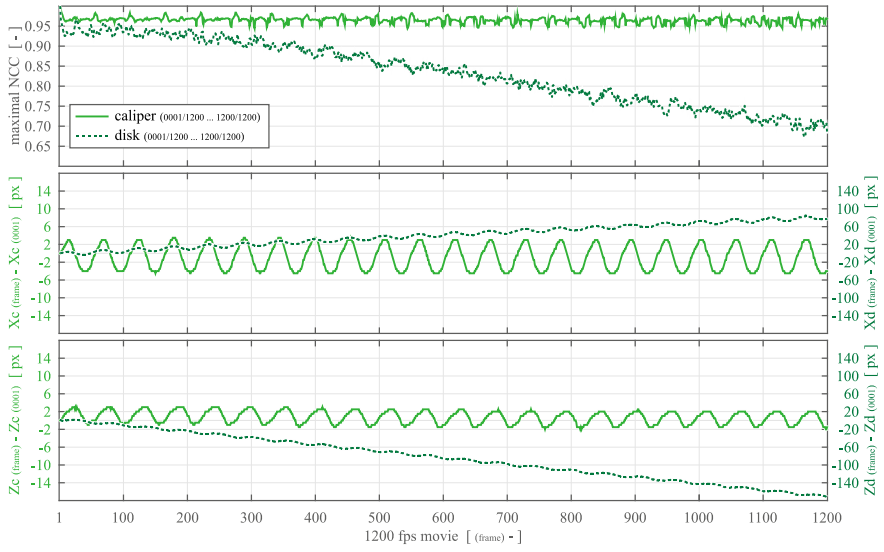
Fig. 8 1200 fps DIC separate template tracking at caliper and disk during 1 s of 22 Hz creep groan: maximal NCC (above), local x-movement (middle), local z-movement (below)
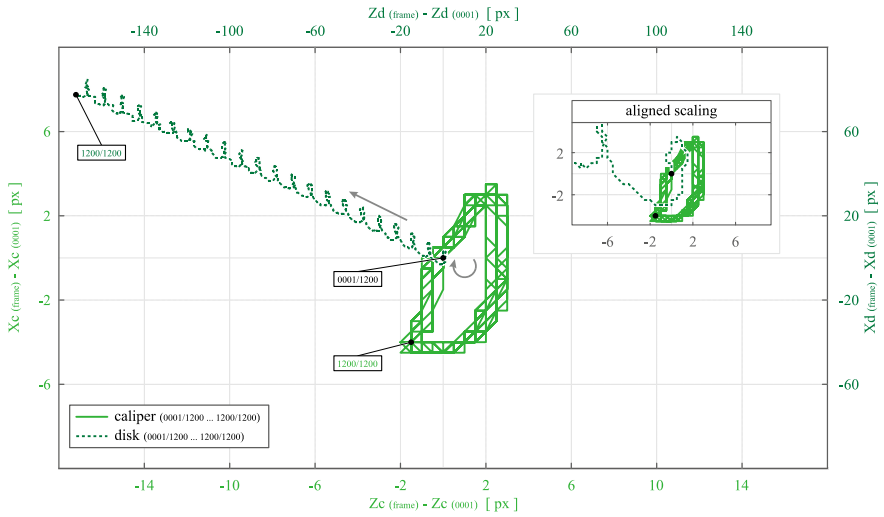

Fig. 9 1200 fps DIC separate template tracking at caliper and disk during 1 s of 22 Hz creep groan: local x- over z-movement
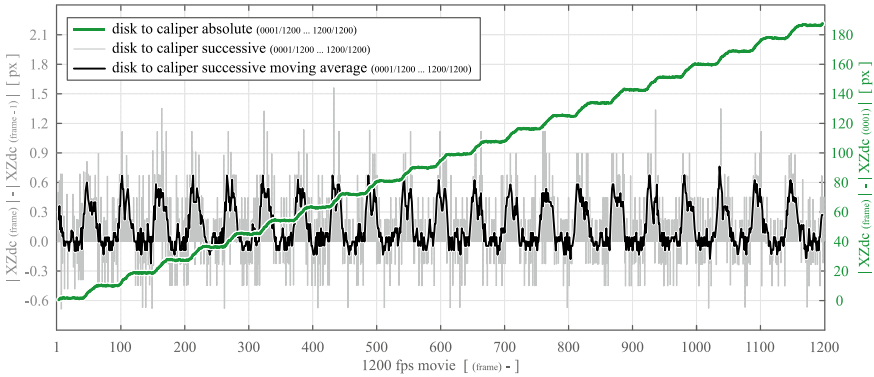
Fig. 10 1200 fps DIC relative template tracking of disk to caliper during 1 s of 22 Hz creep groan: absolute, successive and successive moving average of combined xz-movement
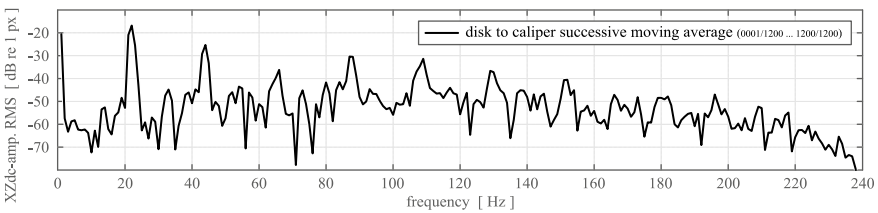

Fig. 11 1200 fps DIC relative template tracking of disk to caliper during 1 s of 22 Hz creep groan: successive moving average FFT frequency content of combined xz-movement RMS

template tracking. Similarity peaks repeatedly appear for intersections of the zx-movement with the preselected starting location. The consistently falling maximal NCC of the disk edge picture series reflects a gradually decreasing DIC reliability. This is the consequence of a continuous perspective distortion and several wandering rim spoke shadows. Both maximal NCC curves have wavy characteristics due to the nonlinear component oscillations. Brake system displacements are visible in the two diagrams of local movements in particular. The ascending calculation reveals amplitudes in x-direction which are nearly twice as large as in z-direction. Spacious longitudinal displacements refer to elasticities in the lower control arm bushings. The disk edge picture series hints at a reasonable circular path with a larger translation in z-direction. This behavior rests on the dictated coordinate system and the observed visual areas. The clockwise rotating x- over z-movement in Fig. 9 facilitates interpretations on alternating tribological states. Temporally and spatially precisely repeated movements consist of coupled pretension orbits during macroscopic stick as well as fragmented relaxation orbits during macroscopic slip. The subplot of aligned scaling shows qualitatively similar system pretension orbits of both separate evaluation threads during the first stick phase. Small orbital differences in these large displacements relate to distance associated deviations between both examined visual

areas. Note that the example begins in the middle of a slip phase and it is completed more than 21 full stick–slip cycles later at the end of a stick phase. Consequently, the basic creep groan frequency is slightly slower than 22 Hz.

1200 fps DIC Relative Template Tracking. A combined evaluation of the disk to caliper relative xz-movement is shown in Fig. 10. The ascending absolute value curve has pronounced staircase characteristics due to the stick–slip intervals. A successive difference value calculation of this staggered curve leads in combination with the described moving average filter to a diagram which is qualitatively comparable to a relative xz-speed. Differences to non-zero values in obvious phases of stick clarify the limitations of the performed DIC approach as a whole. The corresponding frequency content in Fig. 11 indicates a typical spectral signal composition of nonlinear vibration phenomena due to stick–slip or creep groan, respectively. A decrease of the amplitudes toward 240 Hz is caused by the moving average filter.

4.2 Basic Vibration Frequency 22 Hz—Conventional Measurements

Results of the traditional measurements are treated in Figs. 12, 13, 14 and 15. High-speed video segment and measurement data segment are in sync. Thus, the identical 22 Hz creep groan phenomenon is analyzed here.

10000 sps Accelerations. Two segments of the offset-corrected caliper anchor acceleration data are presented in Fig. 12, compared to very similar results in [16, 17]. Steeply increasing peaks, which are negatively signed in x-direction and positive in z-direction, indicate abrupt macroscopic transitions from stick to slip. The strong peaks occur when the wheel assembly suddenly pans rearwards, and simultaneously, the caliper anchor subsystem rotates backwards around the disk axis. Between these primary peaks, a precisely repeated dynamic signature of less intensity reflects phases of slip and the combination of translational relaxation movements with inherent resonances of higher order. The beginning of each continuous stick phase is hinted via a slightly increasing x-acceleration across the zero line. Different amplitudes in both synchronous data segments suggest a higher relevance of the x-direction for this
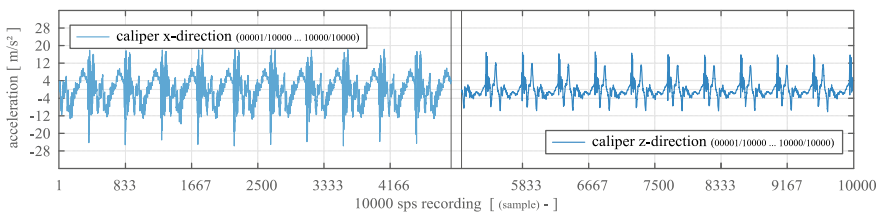

Fig. 12 10,000 sps accelerations measured on the caliper anchor during 1 s of 22 Hz creep groan: local x-acceleration (left) and local z-acceleration (right)
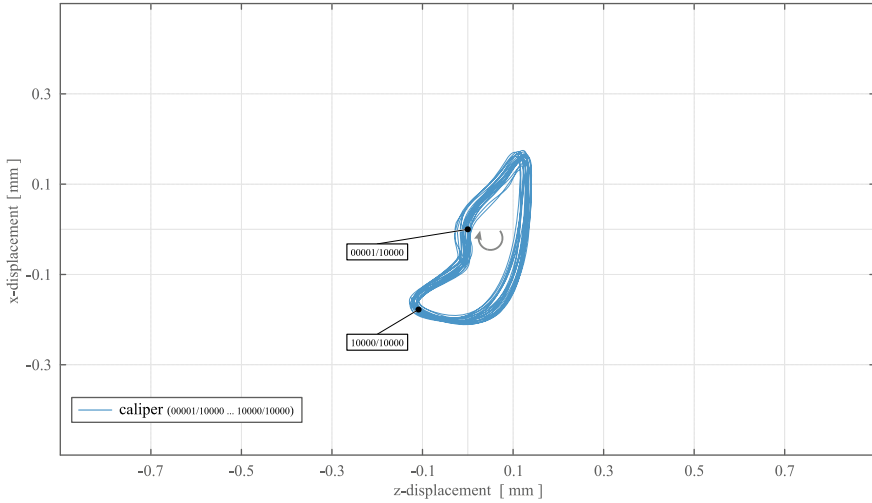
Fig. 13 10,000 sps accelerations measured on the caliper anchor during 1 s of 22 Hz creep groan: local x- over z-movement from numerical double integration
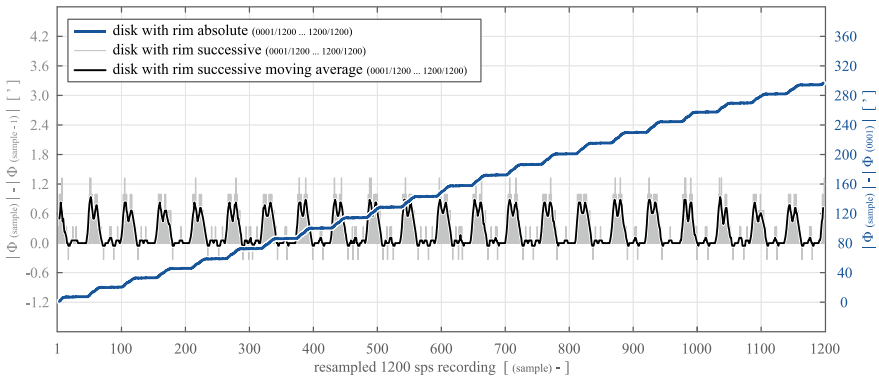

Fig. 14 Resampled 1200 sps disk with rim rotation measured during 1 s of 22 Hz creep groan: absolute, successive and successive moving average of angle
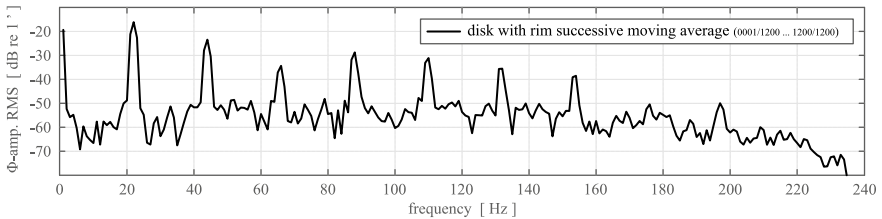

Fig. 15 Resampled 1200 sps disk with rim rotation measured during 1 s of 22 Hz creep groan: successive moving average FFT frequency content of angle RMS

creep groan phenomenon. This inference agrees with the clockwise rotating x- over z-movement in Fig. 13. The temporally and spatially uniformly repeated displacements have qualitatively coequal nonlinear characteristics as a conceivable median orbit of the caliper anchor in Fig. 9. Thus, previous interpretations on alternating tribological states hold true here. Again, the example begins in the middle of a slip phase. It is completed more than 21 full stick–slip cycles later at the end of a stick phase.

Resampled 1200 sps Rotation. The deduced rotation angle of the disk with rim is treated in Fig. 14. Results are in line with Fig. 10. The ascending absolute value curve has also pronounced staircase characteristics. Its smoothed successive difference values, which qualitatively most likely represent the friction couple's tangential relative speed, clearly reflect stick–slip cycles. Double peaks in this metric are caused by inherent resonances of higher order. The corresponding frequency content in Fig. 15 hints at characteristics highly similar to the FFT results in Fig. 11.

4.3 Basic Vibration Frequency 87 Hz—Non-contact Approach

Results of the non-contact approach in Figs. 16, 17, 18 and 19 relate to 87 Hz creep groan which alternatively occurs at 20 bar with 0.10 km/h. Mind that some axis scales are different to the previous example by one power of ten.
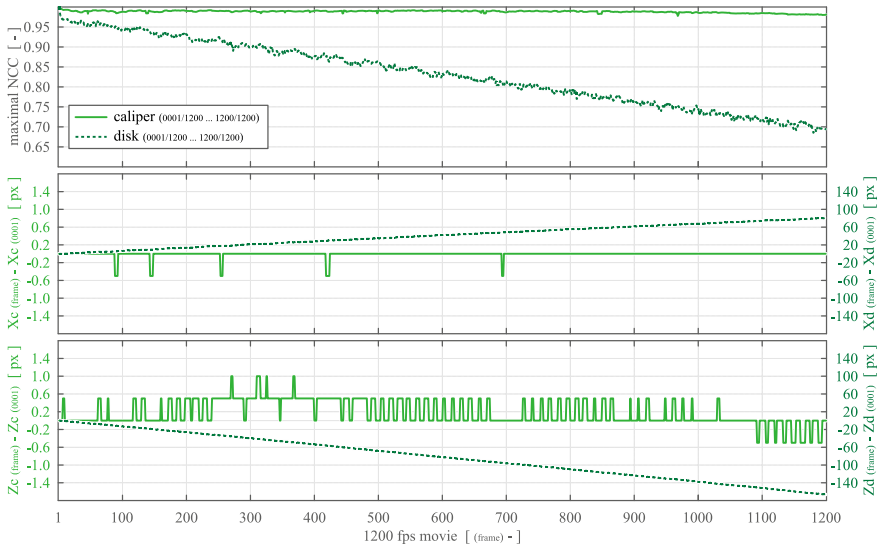

Fig. 16 1200 fps DIC separate template tracking at caliper and disk during 1 s of 87 Hz creep groan: maximal NCC (above), local x-movement (middle), local z-movement (below)
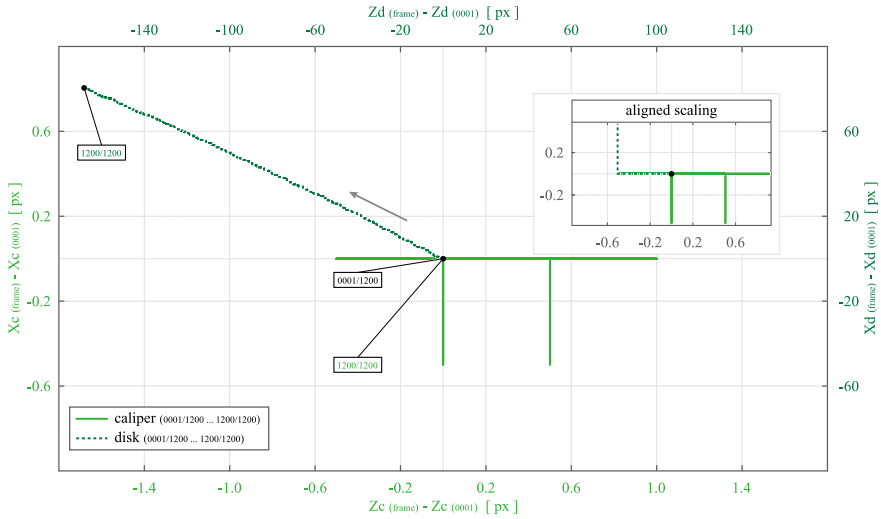
Fig. 17 1200 fps DIC separate template tracking at caliper and disk during 1 s of 87 Hz creep groan: local x- over z-movement
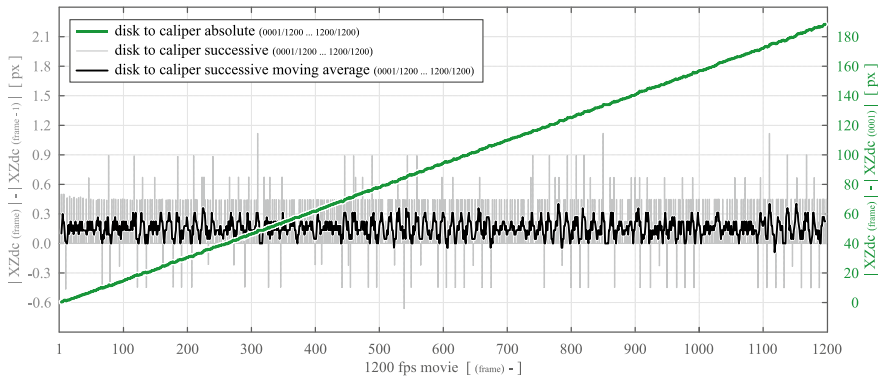

Fig. 18 1200 fps DIC relative template tracking of disk to caliper during 1 s of 87 Hz creep groan: absolute, successive and successive moving average of combined xz-movement
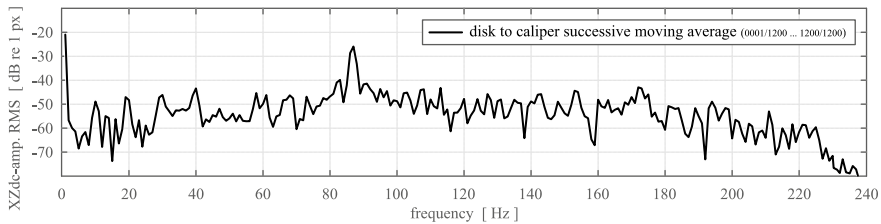

Fig. 19 1200 fps DIC relative template tracking of disk to caliper during 1 s of 87 Hz creep groan: successive moving average FFT frequency content of combined xz-movement RMS
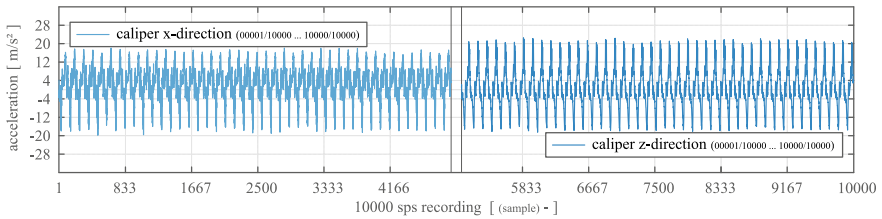
Fig. 20 10,000 sps accelerations measured on the caliper anchor during 1 s of 87 Hz creep groan: local x-acceleration (left) and local z-acceleration (right)

1200 fps DIC Separate Template Tracking. As one can see in Fig. 16, the caliper anchor picture series leads to a consistently high and rather undisturbed maximal NCC curve. It hints at a small zx-movement close to the spatial resolution. Again, perspective distortion as well as rim spoke shadows cause a gradually decreasing maximal NCC regarding the disk edge picture series. The characteristics of this curve are also less wavy here. Consequently, the expected nonlinear brake system oscillations are hardly visible in the diagrams of local movements. The ascending calculation concerning the caliper anchor subsystem mainly indicates amplitudes in z-direction which refer to its rotation around the disk axis. Again, the disk edge picture series suggests a circular path. The local x- over z-movement in Fig. 17 hardly enables interpretations which resemble the quality of the 22 Hz creep groan. Nevertheless, spatially repeated movement patterns appear in the subplot of aligned scaling. It shows qualitatively comparable system pretension paths close to the end of the first stick phase. Mind that a visual resolution of 0.5 px is possible through the mentioned bilinear interpolation.

1200 fps DIC Relative Template Tracking. The combined evaluation can be seen in Fig. 18. The ascending absolute value curve with marginal staircase characteristics has very small and partly interrupted steps. The unsmoothed calculation of successive difference values, which qualitatively suggests a relative xz-speed, allows merely a coarse stick–slip distinction. Tight intervals and negative values clarify the limitations of the performed DIC approach as a whole. Since the centered five-point moving average filter smoothens the signal dynamics, it prevents valid values at zero during phases of stick. Nevertheless, the corresponding frequency content in Fig. 19 indicates at least a correct major vibration interval. A first super-harmonic is already missing due to temporal and spatial restrictions.

4.4 Basic Vibration Frequency 87 Hz—Conventional Measurements

Results of the traditional measurements are shown in Figs. 20, 21, 22 and 23. High-speed video segment and measurement data segment are in sync for the relevant 87 Hz creep groan phenomenon.
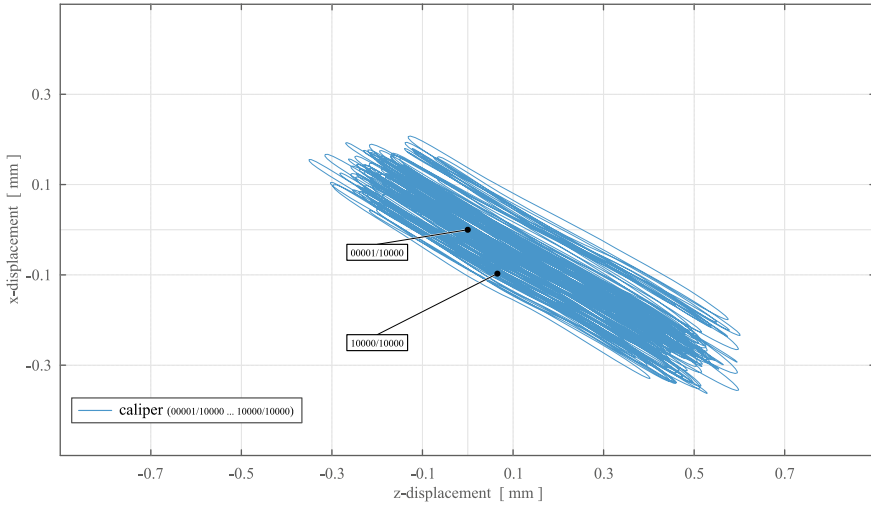
Fig. 21 10,000 sps accelerations measured on the caliper anchor during 1 s of 87 Hz creep groan: local x- over z-movement from numerical double integration
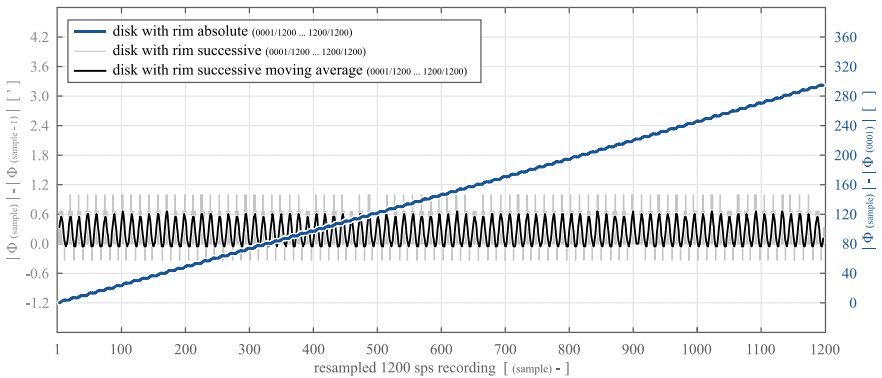

Fig. 22 Resampled 1200 sps disk with rim rotation measured during 1 s of 87 Hz creep groan: absolute, successive and successive moving average of angle
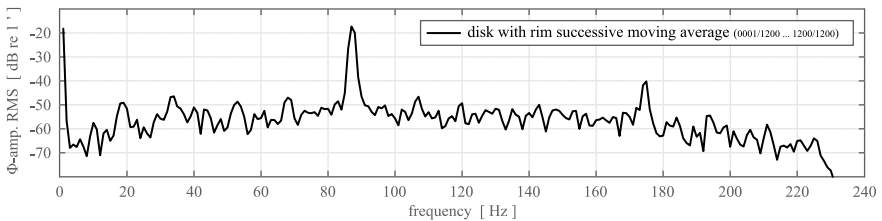

Fig. 23 Resampled 1200 sps disk with rim rotation measured during 1 s of 87 Hz creep groan: successive moving average FFT frequency content of angle RMS

10000 sps Accelerations. The offset-corrected caliper anchor acceleration data is treated in Fig. 20; compare with very similar diagrams in [16, 17]. Primary peaks, which are negative in x-direction and positively signed in z-direction, indicate transitions from stick to slip. The peaks occur when the caliper anchor subsystem suddenly rotates backwards around the disk axis. Between these primary peaks, a precisely repeated signature reflects natural oscillations of higher order. These appear during phases of slip. A flatly increasing x-acceleration across the zero line refers to the beginning of the stick phase. The local x- over z-movement in Fig. 21 shows quantitatively nearly similar displacement amplitudes in both directions. Note that the values refer to a prechosen temporal starting point at an arbitrary spatial starting location which is set to zero. Pretension during macroscopic stick is indicated via the diagonal path to the upper left of the diagram. Relaxation during macroscopic slip is oppositely directed. These nonlinear vibration patterns and stick–slip cycles are hardly identifiable from the caliper anchor picture series; see Fig. 17.

Resampled 1200 sps Rotation. The rotation angle diagrams in Fig. 22 are more meaningful than the results in Fig. 18. Although both ascending absolute value curves have coequal basic properties, stick–slip associated steps are staggered more precise here. Consequently, the smoothed successive difference values reflect these stick–slip cycles akin to a tribological relative speed. Stick phases lead to values near zero. Since coupled rotational movements of the caliper anchor subsystem are not taken into account, the evaluation is biased compared to the real-world stick–slip distinction. Nevertheless, the corresponding frequency content in Fig. 23 indicates the major vibration interval and its first super-harmonic. A decrease of the amplitudes toward 240 Hz is caused by the moving average filter.

5   Conclusions

5.1   Summary of Novel Experimental Creep Groan Investigations

Automobile brake engineers need supplementary experimental NVH investigation methods to fill gaps in current development processes. On that account, this case study has demonstrated the capabilities of a non-contact DIC approach to exemplify, analyze and comprehend subsystem interactions. The 2-D approach has been applied on picture series of an available low-cost high-speed camera which was pointed to the floating caliper disk brake system of a MacPherson-type front axle setup. A drum-driven chassis corner test rig has been used to stimulate two different creep groan phenomena. These had a basic stick–slip frequency around 22 and 87 Hz.

The validated non-contact approach has revealed periodic nonlinear vibrations which are invisible to the human eye. These rely on macroscopic stick–slip transitions of the friction pair and inherent low-frequency resonances of certain chassis corner subsystems. The 22 Hz creep groan involves quasi-static deformations and

dynamic deflections in the lower control arm axle bushings. The nonlinear elasticity properties of the hydro bushing affect the vibration patterns in particular. Furthermore, phases of slip of the spacious 2-D displacement orbits have indicated natural oscillations of higher order as well as caliper subsystem rotations around the disk axis. The MacPherson-type suspension strut assembly, including coil spring, is a significant contributor. Beyond that, its elastic first-order bending deflection facilitates the 87 Hz creep groan. The structural elasticity is transformed to a rotational kinematic displacement of the caliper subsystem, which allows a pronounced stick–slip effect.

Eventually, this case study has verified that customized non-contact DIC methods are helpful for a holistic understanding of brake creep groan. The authors believe that this applies to other low-frequency brake NVH issues alike.

5.2   Recommendations on Non-contact Approach for Current Application

A validation by means of caliper acceleration and disk rotation measurements has revealed fundamental limitations. Although results highly correlate, the implemented DIC approach has not achieved accuracies of the traditional measurements. However, enhancements are possible to meet some basic requirements of brake engineers.

On one hand, the fundamental limitations are caused by an outdated film equipment. The deployed digital high-speed camera offers its best temporal resolution of 1200 fps exclusively in combination with a maximal visual resolution of 336×96 px. Whereas temporal restrictions practically merely diminish the super-harmonics of creep groan vibrations, spatial restrictions minimize the application bandwidth as a whole. Although image interpolation has been performed to overcome some shares of the visual restrictions, this scaling does not replace the quality of a modern recording system. Nowadays, affordable high-speed cameras already provide a high-definition resolution at better sampling rates than used here. Larger visual areas of interest and tracking markers at numerous reasonable positions are enabled thereby.

On the other hand, improvements regarding DIC calculation and/or data processing are possible. Firstly, inclusion of graphics card computations as well as implementation of a so-called fast NCC algorithm, see [33]. Both measures may significantly reduce the computational effort. Secondly, linkage of the results to known object dimensions in the picture series. This suggestion delivers real-world motion quantities. Thirdly, analysis of numerous surface sections instead of singular local areas. This measure enables a detection of rotations and a deduction of field quantities. Fourthly, appropriate result visualizations with animations overlaid to an analyzed high-definition video segment. This suggestion allows more transparent interpretations. Finally, elaboration of an intuitive graphical user interface to facilitate a user-friendly configuration of the digital image processing sequence.

References

1. Barden P (2013) Decoded: the science behind we buy. Wiley, Hoboken. ISBN-13: 978-1118345603
2. Csere C (2011) The trouble with J.D. Power's Initial Quality Study (IQS) with focus on the 2011 U.S. survey. Car and Driver Magazine, Boone. https://www.caranddriver.com/features/a15122465/the-trouble-with-jd-powers-initial-quality-study-feature. Accessed 19 July 2018
3. Youngs J (2014) Top-10 problems in 3-year-old vehicles according to J.D. Power's 2014 U.S. Vehicle Dependability Study (VDS). J.D. Power, Westlake Village. https://www.jdpower.com/cars/articles/jd-power-studies/vehicle-dependability-study-top-10-problems-3-year-old-vehicles. Accessed 19 July 2018
4. Davies GO (2017) Vehicle dependability in Japan declines, J.D. Power's 2017 Study (VDS) finds. Automotive World Ltd, Penarth. https://www.automotiveworld.com/news-releases/vehicle-dependability-japan-declines-j-d-power-finds. Accessed 19 July 2018
5. Schwartz HW, Hays WD, Tarter JH (1985) A systematic approach to the analysis of brake noise. SAE technical paper 850990. https://doi.org/10.4271/850990
6. Abdelhamid MK (1995) Creep groan of disc brakes. SAE technical paper 951282. https://doi.org/10.4271/951282
7. Brecht J, Hoffrichter W, Dohle A (1997) Mechanisms of brake creep groan. SAE technical paper 973026. https://doi.org/10.4271/973026
8. Vadari V, Jackson M (1999) An experimental investigation of disk brake creep-groan in vehicles and brake dynamometer correlation. SAE technical paper 1999-01-3408. https://doi.org/10.4271/1999-01-3408
9. Wu G, Jin S (2014) Combination of test with simulation analysis of brake groan phenomenon. SAE Int J Passeng Cars Mech Syst 7(3):1119–1127. https://doi.org/10.4271/2014-01-0869
10. Suetti AGL, Pederiva R (2015) Phase plane analysis and determination of damping limit in mechanical systems with stick–slip. SAE technical paper 2015-36-0026. https://doi.org/10.4271/2015-36-0026
11. Neis PD, Ferreira NF, Poletto JC, Matozo LT et al (2016) Quantification of brake creep groan in vehicle tests and its relation with stick–slip obtained in laboratory tests. J Sound Vib 369:63–76. https://doi.org/10.1016/j.jsv.2016.01.036
12. Augsburg K, Hauschild P, Gramstat S (2016) Fundamental tests of low-frequency noise phenomena especially creep groan, with a simplified test setup: EB2016-FBR-023. In: Proceedings of EuroBrake Conference and Exhibition, Milan, Italy
13. Meng D, Zhang L, Xu J, Yu Z (2017) A transient dynamic model of brake corner and subsystems for brake creep groan analysis. J Shock Vib 2017, 18. https://doi.org/10.1155/2017/8020797
14. Zhao X, Gräbner N, von Wagner U (2018) Theoretical and experimental investigations of the bifurcation behavior of creep groan of automotive disk brakes. J Theor Appl Mech Pol 56(2):351–364. https://doi.org/10.15632/jtam-pl.56.2.351
15. Pürscher M, Fischer P (2017) Systematic experimental creep groan characterization using a suspension and brake test rig. SAE technical paper 2017-01-2488. https://doi.org/10.4271/2017-01-2488
16. Pürscher M, Huemer-Kals S, Fischer P (2018) Experimental and simulative study of creep groan in terms of MacPherson Axle bushing elasticities: EB2018-SVM-011. In: Proceedings of EuroBrake Conference and Exhibition, The Hague, Netherlands
17. Pürscher M, Huemer-Kals S, Fischer P (2019) Investigations on creep groan concerning static and dynamic axle bushing properties: EB2019-SVM-001. In: Proceedings of EuroBrake Conference and Exhibition, Dresden, Germany
18. Hawkins RD (1954) High-speed motion photography as a tool in shock and vibration. SAE technical paper 540157. https://doi.org/10.4271/540157
19. Belloni V, Ravanelli R, Nascetti A, Di Rita M et al (2018) Digital image correlation from commercial to FOS Software: a mature technique for full-field displacement measurements. Int Arch Photogramm Remote Sens Spatial Inf Sci XLII(2):91–95. https://doi.org/10.5194/isprs-archives-XLII-2-91-2018

20. Orteu JJ (2009) References on applications of DIC to experimental solid mechanics. IMT Mines Albi, Albi. https://www.perso.mines-albi.fr/~jeanjose/DICbib/jjo_DIC.pdf. Accessed 10 Apr 2019
21. Ferrer B, García JI, Roig AB, Mas D (2014) Vibration measurement through high speed vision system in a civil structure under impact loading. AIP Conf Proc 1600(1):190–195. https://doi.org/10.1063/1.4879581
22. Hedayat A, Ashur S (2015) Digital image correlation and its application in an undergraduate civil engineering materials laboratory. In: Proceedings of Illinois-Indiana section conference of american society for engineering education, Fort Wayne, US
23. Tuononen AJ (2014) Digital image correlation to analyse stick–slip behaviour of tyre tread block. Tribol Int 69:70–76. https://doi.org/10.1016/j.triboint.2013.09.003
24. Pesaresi L, Stender M, Ruffini V, Schwingshackl CW (2017) DIC measurement of the kinematics of a friction damper for turbine applications. In: Proceedings of international modal analysis and structural dynamics conference and exposition of society for experimental mechanics, Garden Grove, US
25. Daoud SM, Meghachou M, Hichem A, Vacher P (2014) The 'Stick–Slip' phenomenon during the active earth pressure failure of a granular soil of analogical material. Eng Technol Appl Sci Res 4(1):566–569. https://doi.org/10.5281/zenodo.14031
26. Rudolf M, Rosenau M, Ziegenhagen T, Ludwikowski V et al (2019) Smart speed imaging in digital image correlation: application to seismotectonic scale modeling. Front Earth Sci 6, 11. https://doi.org/10.3389/feart.2018.00248
27. Nonomura Y, Miura T, Miyashita T, Asao Y et al (2012) How to identify water from thickener aqueous solutions by touch. J R Soc Interface 9(71):1216–1223. https://doi.org/10.1098/rsif.2011.0577
28. Van Karsen C, Bouman T, Gwaltney G (2013) Operating deflection shapes of a violin string via high speed/high resolution videography. In: Proceedings of international modal analysis and structural dynamics conference and exposition of society for experimental mechanics, Garden Grove, US
29. Kawabe K, Kawai T, Komoto T, Kuroda S (2012) A study on local compression behavior of brake friction materials by means of digital image correlation method. Sen'i Gakkaishi 68(6):164–171. https://doi.org/10.2115/fiber.68.164
30. Dufrenoy P, Magnier V, Mann R, Cristol AL et al (2016) Methodology linking formulation, microstructure and mechanical properties of friction materials. SAE technical paper 2016-01-1910. https://doi.org/10.4271/2016-01-1910
31. Gieck JE (1965) Studying brake noise with ultra slow motion photography. SAE technical paper 650489. https://doi.org/10.4271/650489
32. Degenstein T (2007) Kraftmessung in Scheibenbremsen: Dissertation Thesis. Technical University, Darmstadt, Germany
33. Lewis JP (1995) Fast normalized cross-correlation. Interval Research, Palo Alto. https://www.scribblethink.org/Work/nvisionInterface/nip.html. Accessed 10 Apr 2019
34. Briechle K, Hanebeck UD (2001) Template matching using fast normalized cross correlation. In: Proceedings of aerospace/defense sensing, simulation, and controls symposium of society for optics and photonics, Orlando, US